ARTICLE

Estimation of valence state and growth rate using principal component analysis of plasma emission in reactive sputtering deposition

Rintaro Minami[a], Eiji Kita[a], Chiharu Mitsumata[a,b], and Hideto Yanagihara[a, b]

[a] Department of Applied Physics, University of Tsukuba, Tsukuba, Ibaraki 305-8573, Japan
[b]Tsukuba Research Center for Energy Materials Science (TREMS), University of Tsukuba, Tsukuba, Ibaraki 305-8573, Japan

ARTICLE HISTORY
Compiled July 24, 2025

ABSTRACT
Reactive sputtering is a complex process in which the valence state of the deposited material and the deposition rate are highly sensitive to growth conditions. Reliable monitoring is essential for achieving reproducible and high-quality thin film growth; however, practical methods remain limited. In this study, we developed a real-time analysis method that combines broad-range plasma emission spectroscopy with principal component analysis (PCA). The results demonstrate that the valence state and deposition rate of iron oxide thin films can be accurately predicted using the first and second principal components. This approach offers a promising tool for real-time prediction and control of the deposition process.

KEYWORDS
machine learning; principal component analysis (PCA); reactive magnetron sputtering; plasma emission spectrum; Mössbauer spectroscopy.

1. Introduction

Thin films of various ceramic compounds, such as oxides and nitrides, are important functional materials. Among the many methods for growing such films, magnetron sputtering is a widely used physical vapor deposition (PVD) techniques both in basic research and industrial applications. Reactive magnetron sputtering enables the growth of a wide range of fascinating oxides and nitrides with diverse compositions and relatively high throughput by controlling the amount of reactive gas such as oxygen or nitrogen. In practice, reactive sputtering is used to produce various functional materials, including TiO_2 [1,2] for photocatalytic and photoelectrochemical applications, TiN and Si_3N_4 [3] for protective coatings, aluminum-doped zinc oxide(AZO) as an alternative to indium tin oxide(ITO) for transparent electrodes [4], and Cu_2O [5] and ZnO [6] for solar cell applications.

A major practical issue in reactive sputtering is the hysteresis observed in the relationship between deposition rate and reactive gas flow. This phenomenon arises

---

CONTACT Chiharu Mitsumata Email: mitsumata.chiharu.fp@u.tsukuba.ac.jp, and Hideto Yanagihara Email: hideto.yanagihara.fm@u.tsukuba.ac.jp

because the target surface transitions between metallic and compound (oxidized or nitrided) states as the reactive gas flow increases or decreases. However, this transition strongly depends on the prior state of the target surface. The sputtering process in the metallic state is referred to as the metallic mode, whereas the sputtering in the compound state is known as the compound mode, or more specifically, the oxide or nitride mode when using oxygen or nitrogen, respectively.

This difference in oxidation or nitridation state of the target surface causes hysteresis in the deposition rate, which has been observed both experimentally [7–12] and theoretically.[13,14] As a results, even under nominally identical deposition conditions, the deposition rate and composition ratio of sputtered thin films can vary, making real-time process control challenging.

In PVD processes, including sputtering, a quartz crystal microbalance is often used to monitor film thickness in real time. This device estimates mass by measuring changes in oscillation frequency caused by accumulating film [15]. However, in reactive sputtering, oxidation and nitridation reactions are highly sensitive to minor environmental fluctuations within the chamber, making accurate real-time film thickness estimation difficult. Empirically, the color of plasma emission during reactive sputtering appears to strongly depend on the amount of reactive gas introduced. This suggests the emission spectrum contains comprehensive information about the ionization states of inert gases, reactive gases, and target species.

In fact, plasma emission analysis has been considered a cost-effective and controllable method for monitoring reactive sputtering, based on techniques developed for conventional non-reactive sputtering.[7,10,16–22]. Previous studies have primarily focused on specific emission lines associated with atoms in the chamber. However, the intensities of these lines result from complex interactions involving emission and absorption by various species in the process environment. Moreover, determining which wavelengths should be monitored remains fundamentally unclear, with no assurance that monitoring only a specific line will adequately capture phenomena such as hysteresis in deposition rate due to changes in reactive gas flow. Therefore, we analyze the entire emission spectrum, by incorporating all available wavelength information rather than focusing on individual lines.

Among various analytical methods, we selected principal component analysis (PCA) for its ability to clearly reveal the relationship between dependent (analysis results) and independent (input data) variables, thereby facilitating interpretation. PCA has already been applied in several pioneering studies in materials science, particularly in plasma-based processes. [23–25]It was used to explore relationships between emission spectra and material properties. In contrast, to this earlier research, this study aims to extract information about the growing film to enable real-time process control.

A suitable prototype compound for this purpose must satisfy two criteria: (1) the valence (oxidation) state should be controllable by adjusting the oxygen flow, and (2) a clear transition between metallic and compound modes should be reflected in measurable physical properties and/or the growth rate. The growth of spinel-type iron oxide thin films by the reactive magnetron sputtering satisfies both criteria. By adjusting the oxygen gas flow rate (ϕ), either Fe_3O_4 (containing mixed-valence Fe^{2+} and Fe^{3+}) or γ-Fe_2O_3 (comprising Fe^{3+} only) can be selectively grown [26], with corresponding differences in growth rate and valence state. In this study we applied PCA to plasma emission spectra measured during deposition, aiming to predict both the valence state and the growth rate of iron oxide thin films. Additionally, we used the PCA results and plasma spectra to derive a physical interpretation of the deposition process.

This article is organized as follows: Section 2 outlines the fabrication method for iron oxide thin films. Section 3 describes the evaluation of valence state and deposition rate. Section 4 presents the PCA results. Finally, Section 5 summarizes the findings of the study.

2. Method

Spinel-type iron oxide thin films were grown using reactive RF magnetron sputtering by introducing O_2 gas into an Ar base gas during film growth. The process temperature was 300°C. Single crystal MgO (001) substrates were used. A 15 sccm Ar gas flow was maintained, while O_2 flow was varied from 0.0 to 1.5 sccm as a growth parameter. The total gas pressure was kept between 1.60 and 1.65 Pa. The RF sputtering power was set to 100 W. After the substrates were heated at 300°C for 1 hour, pre-sputtering was performed for 10 minutes in a 15 sccm Ar flow. Sputtering deposition was then carried out by introducing O_2 gas as a reactive component. Films with thicknesses typically ranging from 30 to 60 nm were grown for various physical property measurements.

Because the reactive sputtering process often exhibits hysteresis between the metallic and the oxide modes, careful control of the target surface state whether metallic or oxidized is essential for ensuring experimental reproducibility. To address this, we conducted film growth experiments using two different deposition procedures, reffered as the ascending process(AP) and descending process(DP) as described in Tables 1.

As shown in Fig. 1, plasma emissions characteristic of the reactive RF magnetron sputtering process during the fabrication of iron oxide samples were observed using a Czerny-Turner-type spectrometer (Thorlabs CCS220). The emissions were collected through a quartz-glass viewport via an optical fiber[27].The viewport is located roughly 50 cm away from the cathode. The spectrum data were integrated and normalized to over one minute.

To characterize the lattice constants and film thicknesses of the grown films, X-ray diffraction (XRD) and X-ray reflectivity (XRR) measurements were performed using Co-K_α radiation. The valence state of the iron oxide films was investigated by conversion electron Mössbauer spectroscopy (CEMS) (see Appendix A). All characterizations were conducted at room temperature. The following sections present the results of these analyses.

3. Experimental Results

3.1. Determination of lattice constants and valence state

The XRD results for all fabricated thin film samples could be categorized into two representative patterns, as shown in Fig. 2. These patterns correspond to samples grown by the DP process at oxygen flow rates of 0.5 sccm and 1.5 sccm, respectively. The results qualitatively agree with previous report [26], indicating that Fe_3O_4 tends to form at lower oxygen flow rates, whereas γ-Fe_2O_3 is more likely to form under higher oxygen flow conditions.

The results of CEMS experiments and analyses are summarized in Appendix A. Representative CEMS spectra are shown in Fig. A1. The oxygen flow dependence of both lattice constants and valence states is summarized in Figs. 3(a) and 3(b), respectively. The data indicate that Fe_3O_4 is obtained at the oxygen flow rate of

0.3 − 0.9 sccm in the AP and 0.3 − 0.8 sccm in the DP. In contrast, γ-Fe_2O_3 is obtained at 1.0 − 1.5 sccm in the AP and at 0.9-1.5 sccm in the DP. Notably, at an oxygen flow rate of 0.9 sccm, significant differences in lattice constants were observed between the two processes, indicating the hysteresis region of the reactive sputtering process.

3.2. Determination of growth rate

Film thickness was measured using XRR method. Fig. 4 shows the calculated growth rates based on film thickness and deposition time at each oxygen flow rate, along with the iron flux rate. As with the valence states and lattice constants, clear hysteresis appears near ϕ =0.9 sccm.This demonstrates that typical characteristics of the reactive sputtering process also appear in this oxide system.[7] The iron flux rate represents the number of iron atoms deposited per square meter per second. At $\phi = 0.9$ sccm, although the oxygen flow rates were identical, noticeable differences in growth rates were observed between the AP and the DP, consistent with differences in lattice constants and valence states. The hysteresis gap is largest at this point, indicating that it corresponds to the transition region discussed in the previous section.

4. Analysis and Discussion

4.1. Dimensional reduction with PCA

As shown in Fig. 5, the plasma emission spectra observed during deposition exhibit numerous peaks, and their intensities depend strongly on the deposition conditions. Machine learning was applied to the spectral data to systematically analyze spectral changes under different sputtering conditions. Since spectral data are functions of wavelength, they form high-dimensional vectors. Thus, PCA was used for dimensionality reduction and feature extraction.

PCA leverages data variance as a feature, and can be implemented using either centralization (focusing on the mean), or standardization (focusing on variance). Since the intensity of plasma emission spectra varies significantly depending on the element or ion species, only centralization was applied in this study. Plasma emission spectra were integrated over a 10-minute period from the onset of deposition. The measured data were preprocessed by normalizing each spectrum to its maximum intensity. Additionally, to address the spectrometer's dynamic range limitations, intensities below 1/300th of the maximum were set to 0 as noise.

The contribution rates of the principal components indicating the proportion of variance retained from the original data, were calculated. The first principal component(PC1) retained 65.5%, PC2 retained 31.2%, PC3 retained 1.5%, and PC4 retained 0.6% of the total variance. The contribution rate dropped significantly from PC3 onward. The cumulative contribution rate for PC1 and PC2 reached 96.7%, indicating that these two components retained sufficient information. Thus, the original 3,648-dimensional data (corresponding to the number of wavelengths) were effectively reduced to two dimensions for subsequent analysis.

4.2. Prediction of valence state and growth rate

An analysis of the valence states of iron oxide thin films under varying oxygen flow rates, as a function of principal component scores, is shown in Fig. 6. Each sample is plotted according to its oxygen flow rate and whether it followed the AP or DP. A linear boundary ($PC2 = 2.308 \times PC1$) separating Fe_3O_4 and γ-Fe_2O_3 regions was determined using a simple perceptron algorithm, as indicated by the dashed line. Samples on the left side of the boundary corresponds to $\gamma-Fe_2O_3$ and those on the right side to Fe_3O_4. The symbols "+" and "×" denote the centroid positions of each group, which serve as reference data derived from machine learning.

Deposition rates (from Fig. 4) were then plotted against PC1 and PC2. Assuming a linear relationship, multiple regression fitting was performed, and the results are shown in Fig 7. Although hysteresis was observed around an oxygen flow rate of 0.9 sccm, the regression yield a high correlation coefficient ($R^2 = 0.89$). Figures 6 and 7 demonstrate that plasma emission spectra can be used to predict deposition rates regardless of the iron oxide phase.

In general, the sputtering deposition rate strongly influenced by input power, with higher power resulting in faster deposition. Under high-power plasma conditions, spectral line intensities increase, making them useful for controlling deposition rates. However, in this study, spectral data were standardized by maximum intensity, meaning that absolute intensity-values were not used. PCA axes are derived from the eigenvectors of the variance-covariance matrix of the data, meaning PCA scores are influenced not only by specific wavelengths but also by the distribution of relative intensities. The successful correlation between PCA scores and deposition rates in this study suggests that relative rather than absolute intensity was dominant facotr. These findings highlight the importance of feature extraction using machine learning for emission-based process control in reactive sputtering.

4.3. PCA Loadings

This section explains the physical significance of the first and second principal components used to estimate valence and deposition rate in the previous section. The principal component loadings represent the elements of the eigenvectors of the variance-covariance matrix of the original data and those indicate the correlation coefficients between the data vectors and the principal component axes. Larger absolute values of the loadings signify a greater contribution from the spectral data at a given wavelength to the corresponding principal component axis. Principal component analysis is a linear mapping of the spatial coordinates representing the data distribution. The contribution to the principal component scores from each wavelength can increase or decrease depending on the loadings. As a result, the scores extract characteristic shape information embedded in the spectral data. The loadings control the degree to which data at specific wavelength increase or decrease the principal component scores. For instance, in two-dimensional space as shown in Fig.6, positive and negative loadings on the PC1 axis correspond to rightward and leftward shifts, respectively, while those on the PC2 axis correspond to upward and downward shifts. The magnitude and sign of the loadings at each wavelength determine the location of a sample in PCA space. Figure 8 shows, the loadings of the first and second principal components across all measured wavelengths. These loadings represent the contributions of all samples, including both Fe_3O_4 and γ-Fe_2O_3.

The wavelengths corresponding to emissions from elements in the material system are compared with the principal component loadings in Fig.9. The elements included are Fe I, Fe II, and Ar, and the emission wavelengths from the NIST database [28] were used as references. The measured wavelengths were grouped into regions (a) through (d) based on differences in emission intensity from each ion. In the short-wavelength region, primarily Fe I emissions were observed, though some emissions did not align with notable features in the loadings (Fig. 9(a)). In Fig. 9(b), contributions from both Fe I and Fe II are present; notably, Fe II around 510 nm and Fe I around 517 nm contribute independently. However, estimating the valence state in this region is difficult, as the PC1 loadings are positive and the PC2 loadings are negative. During deposition, emission spectrum was more intense at wavelengths above 700 nm, as shown in Fig.5. In Figs. 9(c) and 9(d), the dominant emissions originate from Ar, indicating that changes in plasma conditions influenced the principal component loadings in these regions. While these emissions do not directly originate from the deposited material, plasma-state variations during deposition may have affected material valence. For example, the most notable spectral differences between Fig.5(a) and (b) are in the 750 nm and 840 nm regions. Here, the PC1 loading is positive and the PC2 loading is negative. Consequently, the emission intensity in this wavelength range tends to increase when the principal component scores are located in the lower right region of Fig 6. This analysis demonstrates that comparing spectra with machine learning results is effective for material identification. However, a more direct method for estimating material valence remains necessary.

4.4. Inverse transformation from PCA coordinates

This section considers the real-time control of the film deposition process through emission spectrum analysis. In PCA, it is necessary to construct a variance-covariance matrix that includes data collected during film deposition. However, the accumulation of training data reduces computational speed, making real-time control impractical. To address this, a parallel method combining immediate spectral analysis and high-precision machine learning was developed.

First, we describe the mathematical operations required for the inverse transformation. As is well known, PCA is a linear transformation of position vectors in orthogonal space. Let D be the matrix of centered spectral data for all samples. The transformation that maximizes the variance in D is given by,

$$P = DU \tag{1}$$

where U is the matrix whose columns are the normalized eigenvectors of $D^T D$, and D^T denotes the transposed matrix of the data array. This transformation maps the original plasma emission spectra D to the principal component space P. The components of the eigenvectors $\boldsymbol{u}$ that make up U correspond to the PCA loadings described earlier. Since the loadings indicate how much wavelength contributes to a principal component spectrum based on how much each wavelength contributes to a principal component, the inverse transformation of the Eq.(1) reconstructs the spectrum based on features extracted by PCA. The inverse transformation is defined as,

$$D_{\mathrm{rev}} = PU^T \tag{2}$$

where P is the scattered data from each sample. When interpolated data points $\boldsymbol{p}$ are used, the spectrum reconstructed from prinipal component features is given by

$\boldsymbol{d}_{\text{rev}} = \boldsymbol{p}U^T$, which is the feature vector. Because the original matrix D was mean-centered, $\boldsymbol{d}_{\text{rev}}$ must be adjusted by adding back the mean spectral intensity to compare it with actual measured spectra.

In this study, the first and second principal components retain 96.7% of the variance in the original data. Therefore, the emission spectra were reconstructed using only these two components. As shown in Fig.6, the centroid positions of each iron oxide thin film in principal component space were used to compute average emission spectra. Figure. 5(c) and (d) show the results of the inverse transformation of the centroids (PC1,PC2), which characterize the deposition processes of Fe_3O_4 and γ-Fe_2O_3, respectively. These reconstructed spectra, derived via machine learning, serve as representative emission profiles for identifying the emitting plasma during deposition. Note that the spectral difference between Fig. 5(c) and (d) tends to resemble the PC1 loadings (not shown here).

Figure 10 presents the cosine similarity between these reconstructed spectra and experimentally measured spectra obtained during iron oxide thin film deposition. The spectra from all measured samples were used to calculate the similarity to the simulated Fe_3O_4 and γ-Fe_2O_3 spectra. Similarity to Fe_3O_4 is plotted on the horizontal axis, and similarity to γ-Fe_2O_3 is on the vertical axis. Based on the results, spectra falling below the dashed line are identified as Fe_3O_4, whereas those above are identified as γ-Fe_2O_3. These classifications are consistent with Mössbauer spectroscopy results (Table A1), where circles correspond to γ-Fe_2O_3 and triangles to Fe_3O_4, confirming the validity of classification using cosine similarity. Accordingly, the valence of the oxide film can be determined in real time during deposition using pretrained machine learning model. For instance, this enables evaluation of whether the oxygen flow rate is excessive or insufficient, providing feedback on process parameters. However, as illustrated in Fig.10, this approach does not yet support linear-scale control of process parameters in real time. We consider linear-scale process control to be a future issue to be addressed in a separate study.

5. Summary

We addressed the inherent complexity of the reactive sputtering process for iron oxide film growth, where the valence state and deposition rate of thin films are highly sensitive to deposition conditions. A real-time diagnostic method was developed, combining plasma emission spectroscopy over a broad wavelength range with PCA.

The analysis revealed that the valence state and deposition rate of iron oxide thin films can be accurately predicted using only the first and second principal components derived from the emission spectra. This approach remained effective even under typical reactive sputtering conditions exhibiting hysteresis with respect to the reactive gas flow rate, including in the transition region. These findings demonstrate that even complex processes in reactive sputtering can be effectively interpreted and predicted through multivariate analysis of plasma emissions.

This approach not only enhances the physical understanding of the sputtering process but also offers a practical solution for real-time process monitoring and control. Future work will focus on extending this method to other material systems and integrating it with feedback control mechanisms for fully automated deposition processes.

Acknowledgements

Mössbauer studies were performed at the Tandem Accelerator Complex, University of Tsukuba (UTTAC), and the Organization for Open Facility Initiatives, University of Tsukuba. This work was supported by the Japan Society for the Promotion of Science (JSPS) KAKENHI (22H04966, 23K26535, and 24H00408), and in part, by the Advanced Research Infrastructure for Materials and Nanotechnology in Japan (ARIM) of the Ministry of Education, Culture, Sports, Science and Technology (MEXT) of Japan (grant number JPMXP1224BA0008).

References

[1] Lindgren T, Mwabora JM, Avendaño E, et al. Photoelectrochemical and optical properties of Nitrogen doped Titanium dioxide films prepared by reactive DC magnetron sputtering. The Journal of Physical Chemistry B. 2003 Jun; 107(24):5709–5716. Available from: `https://doi.org/10.1021/jp027345j`.

[2] Takeda S, Suzuki S, Odaka H, et al. Photocatalytic TiO_2 thin film deposited onto glass by DC magnetron sputtering. Thin Solid Films. 2001;392(2):338–344. 3rd International Conference on Coatings on Glass (ICCG); Available from: `https://www.sciencedirect.com/science/article/pii/S0040609001010549`.

[3] Chen YH, Lee KW, Chiou WA, et al. Syhnthesis and structure of smooth, superhard TiN/SiN_x multilayer coatings with an equiaxed microstructure. Surface and Coatings Technology. 2001;146-147:209–214. Proceedings of the 28th International Conference on Metallurgic Coatings and Thin Films; Available from: `https://www.sciencedirect.com/science/article/pii/S0257897201013901`.

[4] Minami T. Present status of transparent conducting oxide thin-film development for indium-tin-oxide (ITO) substitutes. Thin Solid Films. 2008; 516(17):5822–5828. 5th International Symposium on Transparent Oxide Thin Films for Electronics and Optics; Available from: `https://www.sciencedirect.com/science/article/pii/S004060900701694X`.

[5] Akimoto K, Ishizuka S, Yanagita M, et al. Thin film deposition of Cu_2O and application for solar cells. Solar Energy. 2006;80(6):715–722. SREN 05 - Solar Renewable Energy News Conference; Available from: `https://www.sciencedirect.com/science/article/pii/S0038092X0500366X`.

[6] Fang Z, Yan Z, Tan Y, et al. Influence of post-annealing treatment on the structure properties of ZnO films. Applied Surface Science. 2005; 241(3):303–308. Available from: `https://www.sciencedirect.com/science/article/pii/S0169433204012486`.

[7] Safi I. Recent aspects concerning DC reactive magnetron sputtering of thin films: a review. Surface and Coatings Technology. 2000;127(2):203–218. Available from: `https://www.sciencedirect.com/science/article/pii/S0257897200005661`.

[8] Aubry E, Weber S, Billard A, et al. Silicon oxynitride thin films synthesised by the reactive gas pulsing process using rectangular pulses. Applied Surface Science. 2011;257(23):10065–10071. Available from: `https://www.sciencedirect.com/science/article/pii/S0169433211010300`.

[9] Musil J, Baroch P, Vlek J, et al. Reactive magnetron sputtering of thin films: present status and trends. Thin Solid Films. 2005;475(1):208–218. Asian-European International Conference on Plasma Surface Engineering 2003 Proceedings of the 4th Asian-European International Conference on Plasma Surface En-

gineering; Available from: `https://www.sciencedirect.com/science/article/pii/S0040609004009332`.

[10] Schiller S, Heisig U, Korndrfer C, et al. Reactive d.c. high-rate sputtering as production technology. Surface and Coatings Technology. 1987;33:405–423. Available from: `https://www.sciencedirect.com/science/article/pii/0257897287902064`.

[11] Spencer A, Howson R, Lewin R. Pressure stability in reactive magnetron sputtering. Thin Solid Films. 1988;158(1):141–149. Available from: `https://www.sciencedirect.com/science/article/pii/0040609088903100`.

[12] Okamoto A, Serikawa T. Reactive sputtering characteristics of silicon in an ArN_2 mixture. Thin Solid Films. 1986;137(1):143–151. Available from: `https://www.sciencedirect.com/science/article/pii/0040609086902026`.

[13] Berg S, Nyberg T. Fundamental understanding and modeling of reactive sputtering processes. Thin Solid Films. 2005;476(2):215–230. Available from: `https://www.sciencedirect.com/science/article/pii/S0040609004016876`.

[14] Strijckmans K, Schelfhout R, Depla D. Tutorial: Hysteresis during the reactive magnetron sputtering process. Journal of Applied Physics. 2018 Dec;124:241101.

[15] Sauerbrey G. Phys verhandl. 1957;8:113.

[16] Rydosz A, Kollbek K, Kim-Ngan NTH, et al. Optical diagnostics of the magnetron sputtering process of copper in an argon–oxygen atmosphere. Journal of Materials Science: Materials in Electronics. 2020 Jul;31(14):11624–11636. Available from: `https://doi.org/10.1007/s10854-020-03713-z`.

[17] Pana I, Vitelaru C, Zoita NC, et al. Tunable optical properties of SiN thin films by OES monitoring in a reactive RF magnetron plasma. Plasma Processes and Polymers. 2016;13(2):208–216. Available from: `https://onlinelibrary.wiley.com/doi/abs/10.1002/ppap.201400202`.

[18] Wang Q, chun Ba D, chen Zhang Y, et al. An investigation on hysteresis process of zno film deposition and changes of surface morphology and wettability. Materials Letters. 2012;68:320–323. Available from: `https://www.sciencedirect.com/science/article/pii/S0167577X11012523`.

[19] Salhi M, Abaidia S, Mammeri S, et al. Sputter deposition of Titanium and Nickel thin films in radio frequency magnetron discharge characterized by optical emission spectroscopy and by Rutherford backscattering spectrometry. Thin Solid Films. 2017;629:22–27. Available from: `https://www.sciencedirect.com/science/article/pii/S0040609017302158`.

[20] Jung MJ, Nam KH, Shaginyan LR, et al. Deposition of Ti thin film using the magnetron sputtering method. Thin Solid Films. 2003;435(1):145–149. Proceedings of the Joint International Plasma Symposium of the 6th APCPST, the 15th SPSM and the 11th Kapra Symposia; Available from: `https://www.sciencedirect.com/science/article/pii/S0040609003003444`.

[21] Iljinas A, Mockeviius I, Andruleviius M, et al. Growth of ITO thin films by magnetron sputtering: OES study, opticaland electrical properties. Vacuum. 2009; 83:S118–S120. Proceedings of the seventh International Conference on Ion Implantation and other Applications of Ions and Electrons (ION 2008),16-19 June 2008, Kazimierz Dolny, Poland; Available from: `https://www.sciencedirect.com/science/article/pii/S0042207X09000645`.

[22] Zhao MJ, Huang J, Li HC, et al. Crystal phase control of copper oxide thin films by process pressure during high power impulse magnetron sputtering. Journal of Science: Advanced Materials and Devices. 2024;9(2):100672. Available from: `https://www.sciencedirect.com/science/article/pii/S2468217924000030`.

[23] Nauschütt BT, Chen L, Holste K, et al. Non-invasive assessment of plasma parameters inside an ion thruster combining optical emission spectroscopy and principal component analysis. EPJ Techniques and Instrumentation. 2021 Aug;8(1):13. Available from: `https://doi.org/10.1140/epjti/s40485-021-00070-x`.

[24] Huang HJ, Kau LH, Wang HS, et al. Large-scale data analysis of pecvd amorphous silicon interface passivation layer via the optical emission spectra for parameterized pca. The International Journal of Advanced Manufacturing Technology. 2019 Mar;101(1):329–337. Available from: `https://doi.org/10.1007/s00170-018-2938-1`.

[25] Lu TY, Yang YP, Lo HH, et al. Minimizing film residual stress with in situ OES big data using principal component analysis of deposited AlN films by pulsed DC reactive sputtering. The International Journal of Advanced Manufacturing Technology. 2021 Jun;114(7):1975–1990. Available from: `https://doi.org/10.1007/s00170-021-07003-8`.

[26] Yanagihara H, Myoka M, Isaka D, et al. Selective growth of Fe_3O_4 and γ-Fe_2O_3 films with reactive magnetron sputtering. Journal of Physics D: Applied Physics. 2013 Apr;46(17):175004. Available from: `https://dx.doi.org/10.1088/0022-3727/46/17/175004`.

[27] Koyama T, Ohmori T, Shibata N, et al. In situ monitoring of zn* and mg* species during helicon-wave-excited-plasma sputtering epitaxy of zno and mg0.06zn0.94o films. Journal of Vacuum Science & Technology B: Microelectronics and Nanometer Structures Processing, Measurement, and Phenomena. 2004 08;22(4):2220–2225. Available from: `https://doi.org/10.1116/1.1768522`.

[28] Kramida A, Ralchenko Y, Reader J, et al. NIST atomic spectra database (version 5.12), [online]. Available: https://physicsnistgov/asd [Sat May 03 2025] National Institute of Standards and Technology, Gaithersburg, MD DOI: https://doiorg/1018434/T4W30F. 2024;.

[29] Gütlich P, Bill E, Trautwein AX. Mössbauer spectroscopy and transition metal chemistry. London: Springer-Verlag; 2011.

[30] Greenwood NN, Gibb TC. Mössbauer spectroscopy. London: Chapman and Hall Ltd; 1971.

[31] Margulies DT, Parker FT, Rudee ML, et al. Origin of the anomalous magnetic behavior in single crystal Fe_3O_4 films. Phys Rev Lett. 1997 Dec;79:5162–5165. Available from: `https://link.aps.org/doi/10.1103/PhysRevLett.79.5162`.

[32] da Costa GM, De Grave E, Vandenberghe RE. Mössbauer studies of magnetite and al-substituted maghemites. Hyperfine Interactions. 1998 Dec;117(1):207–243. Available from: `https://doi.org/10.1023/A:1012691209853`.

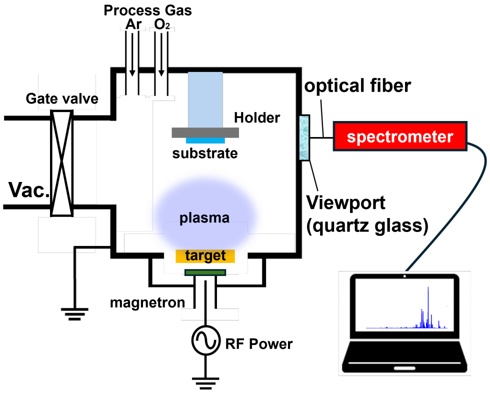

Figure 1. Schematic diagram of the RF magnetron sputtering system. Plasma emission spectra were collected by a spectrometer through a quartz-glass viewport via an optical fiber.

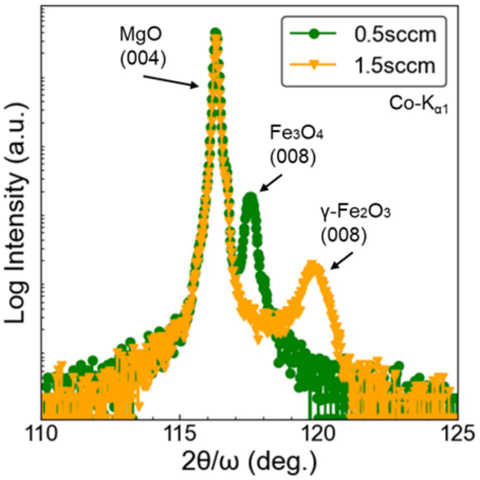

Figure 2. Typical XRD patterns around the MgO(004) peak. Green circles and yellow triangles represent results at oxygen flow rates of 0.5 sccm and 1.5 sccm, respectively.

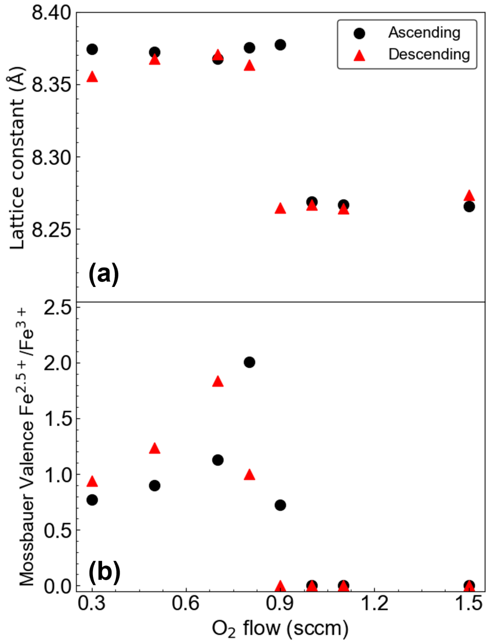

Figure 3. O_2 flow dependence of (a) lattice constants and (b) valence ratios from CEMS for reactively sputtered iron oxide thin films. Solid circles and triangles correspond to samples from the AP and DP, respectively.

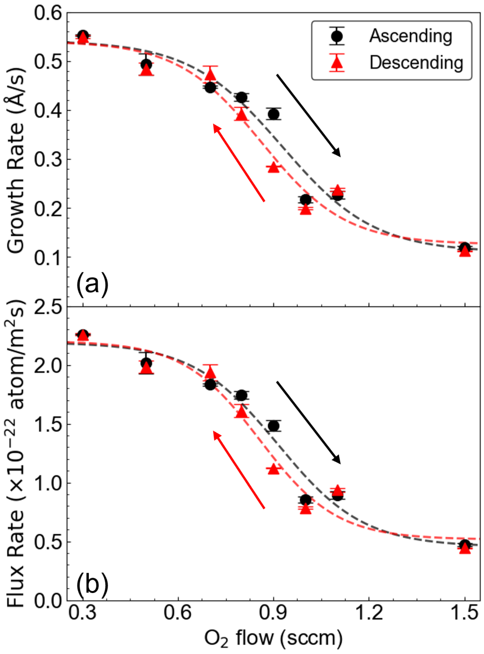

Figure 4. Growth characteristics of the iron oxide thin films. Black circles represent AP results, and red triangles represent DP results. (a) Deposition rate at each oxygen flow rate. (b) Iron flux rate at each oxygen flow rate. The fitting curves are visual guides.

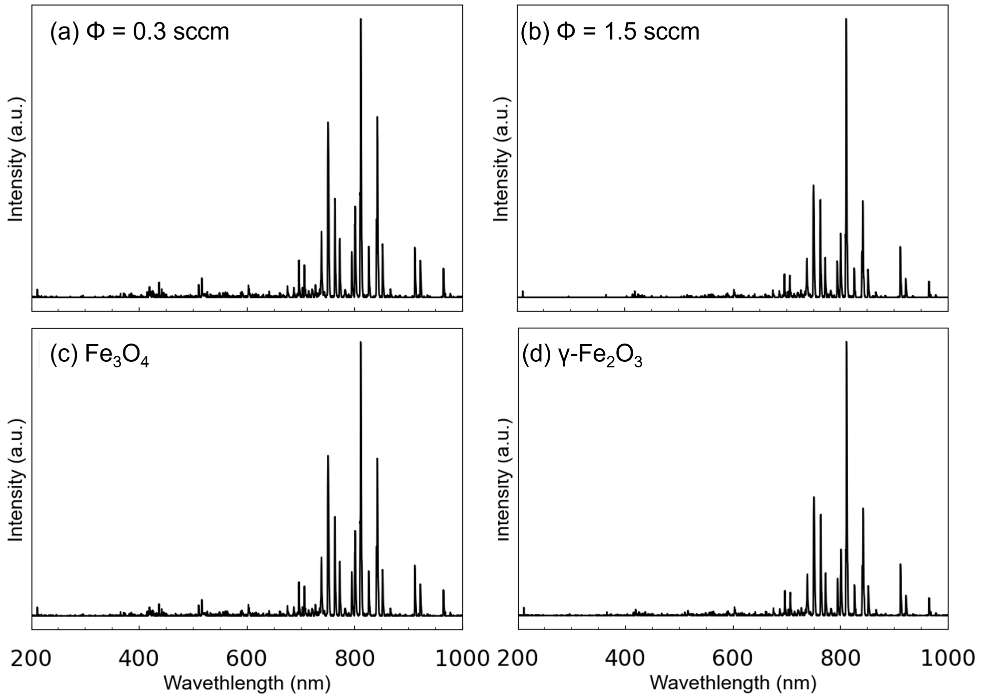

Figure 5. Plasma emission spectra observed during the fabrication of iron oxide samples using the AP (wavelength range: 200-1000 nm). (a) Spectrum at an oxygen flow rate of 0.3 sccm. (b) Spectrum at an oxygen flow rate of 1.5 sccm. (c) PCA-inverse-transformed spectrum at the centroid of Fe_3O_4. (d) PCA-inverse-transformed spectrum at the centroid of γ-Fe_2O_3.

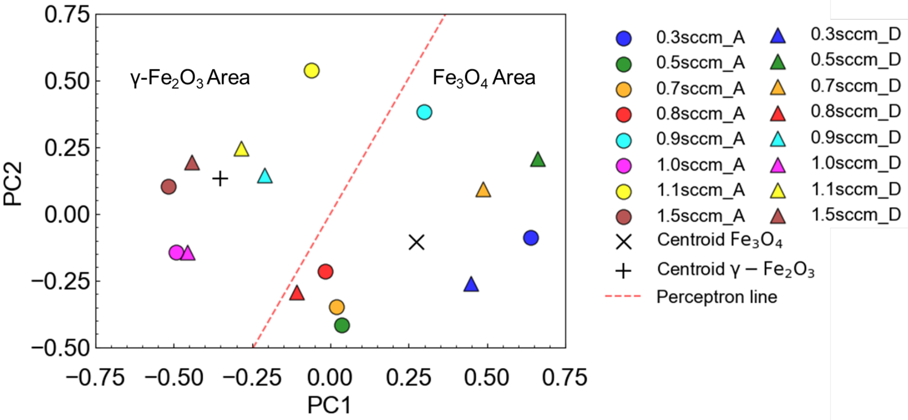

Figure 6. Iron oxide samples plotted in principal component space using the first and second principal components. Circles represent samples from the AP; triangles represent those from the DP. The symbols ”+” and ”×” indicate centroid positions for $\gamma-Fe_2O_3$ and Fe_3O_4, respectively. The dashed line is the perceptron derived boundary separating the two compounds.

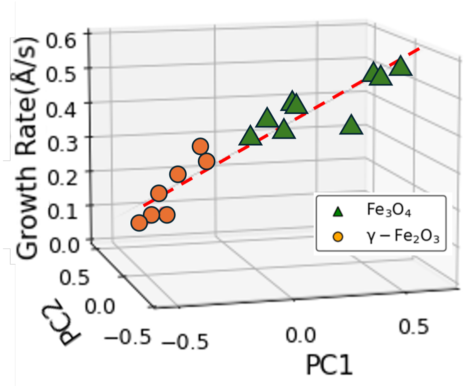

Figure 7. Prediction of growth rate using the first and second principal components. A multiple regression analysis was performed to derive a first-order polynomial for predicting growth rate. The growth rate z [Å/s] is expressed using PC1 (x) and PC2 (y) as $z = 0.34 - 0.30x - 0.23y$, shown by the dashed line. Circles represent γ-Fe_2O_3 thin films, whereas triangles represent Fe_3O_4 thin films.

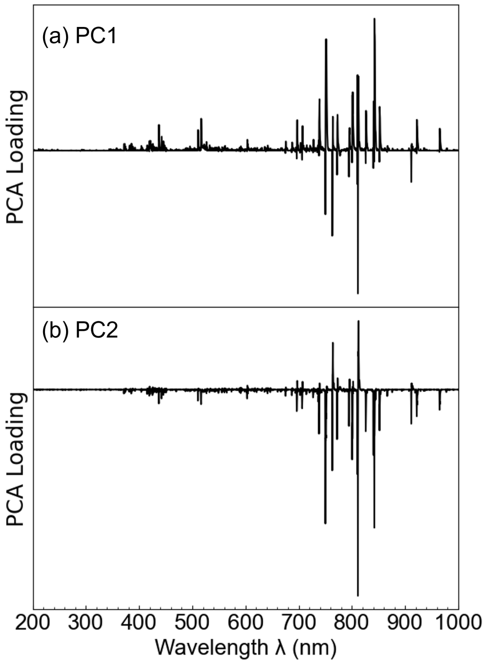

Figure 8. Principal component loadings at each wavelength (wavelength range: $200-1000$nm) for (a) PC1 and (b) PC2.

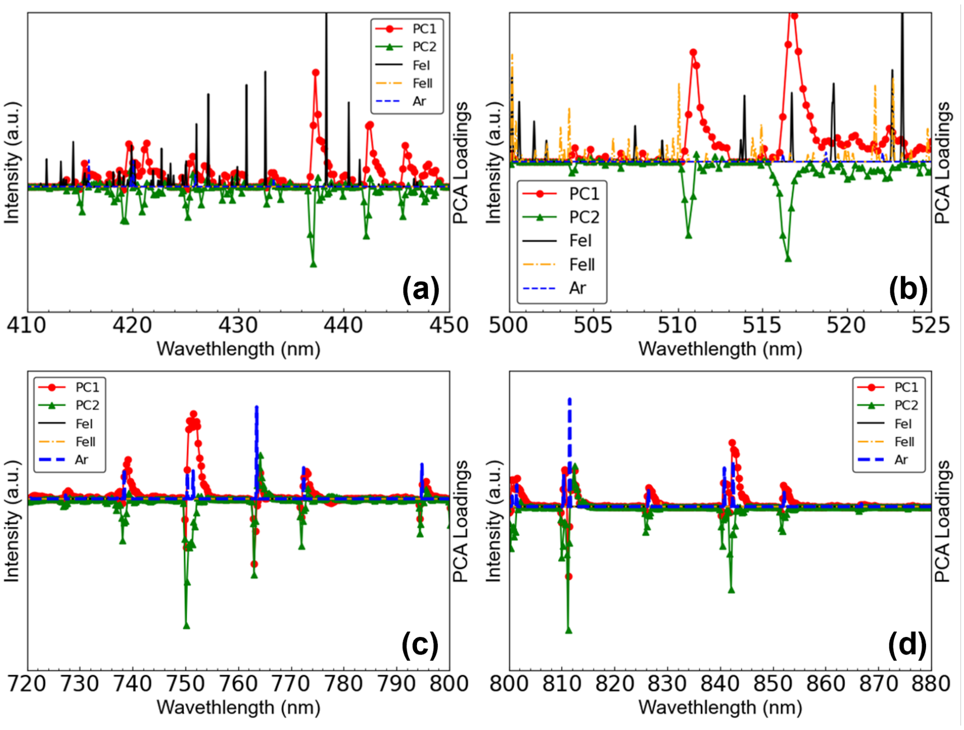

Figure 9. Comparison of principal component loadings and emission wavelengths of Fe I (neutral Fe atoms), Fe II (Fe^+ ions), and Ar. Short-wavelength regions: (a) $410-450$nm, (b) $500-525$nm. Long-wavelength regions: (c) $720-800$nm, (d) $800-880$nm.

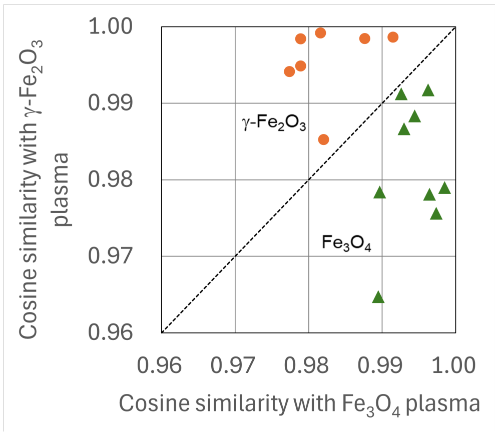

Figure 10. Cosine similarity between the plasma emission spectra measured during iron oxide thin film fabrication and the simulated spectra obtained by inverse transformation from the centroids in Fig. 6.

Table 1. Deposition procedures for AP and DP. The pre-sputtering steps PS1 and PS1-1 remove surface oxides from the target. PS1-2 forms a sufficiently thick oxide layer on the target surface. PS2 stabilizes the surface oxide under steady-state conditions at a predetermined oxygen flow rate.

	Process step	O_2 flow rate (sccm)	Duration (min)
AP	PS1	0.0	10.0
	PS2	Set value	10.0
	Film growth	Set value	Appropriate time
DP	PS1-1	0.0	10.0
	PS1-2	2.0	10.0
	PS2	Set value	5.0
	Film growth	Set value	Appropriate time

Appendix A. Valence state determination

To evaluate the valence states of the fabricated iron oxide thin films, conversion electron Mössbauer spectroscopy (CEMS) was used. While traditional Mössbauer spectroscopy counts transmitted γ-rays, the CEMS technique [29] measures internal conversion electrons ejected following the resonant absorption of γ-rays. With a maximum escape depth of about 100 nm, this method is well-suited for thin film measurements, and was used for measurements of iron oxide thin films [26]. A conventional CEMS counter was employed, and spectra recorded at room temperature were analyzed using commercially available fitting software (MossWinn 4.0). Mössbauer parameters of hyperfine fields (H_{hf}), isomer shifts (δ) and subspectral area ratios were extracted from the fits. Figure A1 shows the CEMS spectra recorded at room temperature and their fitted results for iron oxide samples fabricated under the Ascending Process.

(1) **Oxygen Flow Rate: 0.3 sccm** The spectrum in Fig. A1 (a) consists of two sextets with internal magnetic fields of approximately 500 kOe and 450 kOe. These values along with the isomer shifts, correspond to the A and B sites of the spinel structure of Fe_3O_4 [30]. Confirming its presence of Fe_3O_4 in the thin film [31].

(2) **Oxygen Flow Rate: 1.5 sccm** The spectrum in Fig. A1 (b) is characterized by a single sextet around 500 kOe, indicating the presence of γ-Fe_2O_3[30]. This oxide contains only Fe^{3+} ions and shows nearly identical magnetic fields and isomer shifts for both A and B sites, making it difficult to distinguish between them. The absence of spectral peaks near 450 kOe confirms that the film consists solely of γ-Fe_2O_3 [32].

For other samples, the spectra could be categorized as either Fe_3O_4 as in Fig. A1 (a) or γ-Fe_2O_3 as in Fig. A1(b), and the corresponding fitting parameters are listed in Table A1. The ratios of $Fe^{2.5+}$ and Fe^{3+} were evaluated from the fit results and are shown in Fig. 3 (b). In Fe_3O_4, the A sites are occupied by Fe^{3+}, whereas the B sites are occupied by equal amounts of Fe^{2+} and Fe^{3+}, namely $Fe^{2.5+}$. The Fe^{2+}/Fe^{3+} ratio in Fe_3O_4 samples was estimated from the area ratio of A and B sites.

Based on Table A1 and Fig. 3, the results are summarized as follows:

- In the **Ascending Process**, Fe_3O_4 is formed at oxygen flow rates of 0.3 – 0.9 sccm, and γ-Fe_2O_3 is formed at 1.0 – 1.5 sccm.
- In the **Descending Process**, Fe_3O_4 is formed at oxygen flow rates of 0.3 – 0.8 sccm, and γ-Fe_2O_3 is formed at 0.9 – 1.5 sccm.

Notably, at an oxygen flow rate of 0.9 sccm, the lattice constants and valence states differ depending on the deposition process. At low oxygen flow rates, Fe is sputtered from the target in metallic form (metal mode) and reacts with oxygen on the substrate to form Fe_3O_4, which has a lower oxidation state. At high flow rates, the target surface becomes oxidized (compound mode), and oxidized iron is sputtered and further reacts with oxygen on the substrate, resulting in γ-Fe_2O_3 with a higher oxidation state.

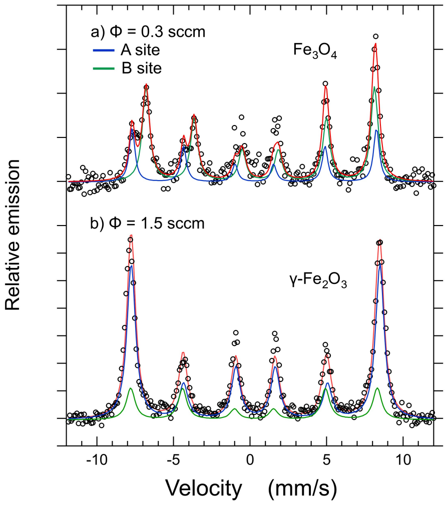

Figure A1. Representative CEMS spectra for iron oxide samples. The circles represent experimental data, and the red lines indicate fitted results. (a) Spectrum of the sample grown at an oxygen flow rate of 0.3 sccm. The green and blue lines correspond to the fitted components for the A site (Fe^{3+}) and B site ($Fe^{2.5+}$), respectively. (b) Spectrum of the sample grown at an oxygen flow rate of 1.5 sccm, fitted assuming a single valence state of Fe^{3+}.

Table A1. Mössbauer fitting parameters for reactively sputtered Fe oxide thin films

	Ascending Process						Descending Process					
O_2 flow	H_{hf} (kOe)		δ* (mm/s)		Area (%)		H_{hf} (kOe)		δ* (mm/s)		Area (%)	
(sccm)	A	B	A	B	A	B	A	B	A	B	A	B
0.3	505	466	0.43	0.66	56.4	43.6	505	467	0.40	0.68	51.6	48.5
0.5	503	464	0.41	0.66	52.7	47.3	503	466	0.36	0.64	44.8	55.2
0.7	503	465	0.36	0.67	47.0	53.0	490	459	0.28	0.66	35.2	64.8
0.8	491	460	0.26	0.64	33.3	66.7	496	464	0.30	0.66	49.9	50.1
0.9	496	464	0.36	0.67	57.9	42.1	507		0.31		100	
1.0	501		0.38		100		501		0.26		100	
1.1	514		0.35		100		505		0.36		100	
1.5	501		0.38		100		501		0.38		100	

*δ : Isomer shift relative to α-Fe.